Title
Identifying different stacking sequences in few-layer CVD-grown MoS2 by low-energy atomic-resolution scanning transmission electron microscopy

Journal
Physical Review B, 93(4)

ISSN
2469-9950

Authors
Yan, Aiming
Chen, Wei
Ophus, Colin
et al.

Publication Date
2016

DOI
10.1103/physrevb.93.041420

Peer reviewed

PHYSICAL REVIEW B **93**, 041420(R) (2016)

Identifying different stacking sequences in few-layer CVD-grown MoS_2 by low-energy atomic-resolution scanning transmission electron microscopy

Aiming Yan,[1,6,7] Wei Chen,[2,4] Colin Ophus,[3] Jim Ciston,[3] Yuyuan Lin,[5] Kristin Persson,[2] and Alex Zettl[1,6,7,*]

[1]*Department of Physics, University of California, Berkeley, California 94720, USA*
[2]*Electrochemical Technologies Group, Lawrence Berkeley National Laboratory, Berkeley, California 94720, USA*
[3]*National Center for Electron Microscopy, Molecular Foundry, Lawrence Berkeley National Laboratory, Berkeley, California 94720, USA*
[4]*Department of Mechanical, Materials and Aerospace Engineering, Illinois Institute of Technology, Chicago, Illinois 60616, USA*
[5]*Department of Materials Science and Engineering, Northwestern University, Evanston, Illinois 60208, USA*
[6]*Materials Sciences Division, Lawrence Berkeley National Laboratory, Berkeley, California 94720, USA*
[7]*Kavli Energy NanoSciences Institute at the University of California, Berkeley and the Lawrence Berkeley National Laboratory, Berkeley, California 94720, USA*

(Received 18 September 2015; revised manuscript received 24 November 2015; published 25 January 2016)

Atomically thin MoS_2 grown by chemical vapor deposition (CVD) is a promising candidate for next-generation electronics due to inherent CVD scalability and controllability. However, it is well known that the stacking sequence in few-layer MoS_2 can significantly impact electrical and optical properties. Herein we report different intrinsic stacking sequences in CVD-grown few-layer MoS_2 obtained by atomic-resolution annular-dark-field imaging in an aberration-corrected scanning transmission electron microscope operated at 50 keV. Trilayer MoS_2 displays a new stacking sequence distinct from the commonly observed 2*H* and 3*R* phases of MoS_2. Density functional theory is used to examine the stability of different stacking sequences, and the findings are consistent with our experimental observations.

DOI: 10.1103/PhysRevB.93.041420

I. INTRODUCTION

Atomically thin molybdenum disulfide (MoS_2) has recently attracted significant attention due to its novel physical and electrical properties. Single-layer MoS_2 (extracted from naturally occurring 2*H*-phase material) has a direct electronic band gap ~1.8 eV [1,2] while bulk 2*H*-phase MoS_2 exhibits a lower indirect band gap ~1.3 eV [3]. This semiconducting nature has been exploited to create MoS_2 field effect transistors (FETs) [4] with a high on-off ratio and ultrasensitive photodetectors [5], among other optoelectronic and photonic [6,7] devices. The number of layers not only provides tunability of the band gap of MoS_2 for photonic applications [8], but also performance enhancements that may not be directly gap related. For instance, the gas sensing behavior of few-layer thick MoS_2 has been found to be better than that of single-layer MoS_2 due to the instability of the single-layer form in reactive gas environments [9,10]. Another example is that few-layer MoS_2 usually displays a higher carrier mobility than that of single-layer MoS_2 in various heterostructured FET configurations [11–13].

The stacking sequence is a major structural factor that controls the properties of few-layer MoS_2. Theoretical calculations have predicted that the stacking sequence in bilayer MoS_2 plays an important role in its electronic band structure [14]. Experimental studies have found that the relative rotation angle in bilayer MoS_2 significantly modifies the direct/indirect band gap and interlayer coupling [15,16]. The recently observed spin/valley polarization in symmetry-breaking 3*R*-phase bulk MoS_2 (another commonly observed phase of bulk MoS_2) further elucidates the key role of stacking sequences (or crystal structure) in the properties of layered MoS_2 [17].

Single- and few-layer MoS_2 grown by chemical vapor deposition (CVD) methods have great potential in building next-generation electronics due to the inherent controllability and scalability [18,19] of CVD growth. A thorough understanding of the structure of CVD-grown MoS_2 is essential for a full exploration of its applications. Here, we demonstrate a precise determination of different stacking sequences in CVD-grown few-layer MoS_2 by employing atomic-resolution annular-dark-field (ADF) imaging in scanning transmission electron microscopy (STEM) using an unusually low electron beam energy (50 keV). Notably, this energy is much lower than the 80 keV threshhold for knock-on damage to MoS_2 [20]; this allows for an extended study of pristine multilayer MoS_2 at the atomic scale. We find that the stacking sequence in CVD-grown MoS_2 is layer dependent, and can be a mixture of 2*H* and 3*R* phases of MoS_2 in trilayer form. Density functional theory (DFT) calculations confirm that the stacking sequences observed in our CVD-grown few-layer MoS_2 are among the most stable configurations.

II. EXPERIMENTAL AND THEORETICAL DETAILS

We use a two-zone furnace to grow single- and few-layer (bilayer and trilayer) MoS_2 on SiO_2/Si substrates, as described previously [21]. A quartz tube contains S and MoO_3 precursors, with S in zone 1 and MoO_3 precursor in zone 2. SiO_2/Si chips are placed on top of the crucible that contains the MoO_3 precursor. N_2 gas flows through the quartz tube during the whole growth process. Zones 1 and 2 are first kept at 105 °C for 3 h to warm up the precursors and 200 sccm N_2 flows through the tube. The temperature of zone 2 is then slowly increased to 500 °C (over 30 min) while zone 1 is kept at 105 °C. These temperatures are maintained for 30 min. The temperatures of zones 1 and 2 are then raised to 400 and 780 °C

*Corresponding author: azettl@berkeley.edu

RAPID COMMUNICATIONS

(over 30 min), respectively, and N_2 flow rate is changed to 9 sccm. The 400 and 780 °C temperatures are maintained for 10 min, after which the furnace is turned off and cooled to room temperature naturally.

We use optical microscopy and Raman spectroscopy to initially characterize single- and few-layer MoS_2 grown on SiO_2/Si by the CVD method (see examples shown in Supplemental Material Sec. 1 [22]) before transferring the flakes onto Quantifoil® TEM grids. Previous studies have shown that single-layer MoS_2 grown on SiO_2/Si by the CVD method displays a direct band gap and shows a strong photoluminescence (PL) peak centered around 1.84 eV at room temperature [18,19]. Double-layer CVD-grown MoS_2 has an indirect band gap and shows a slightly redshifted PL peak compared to the single-layer form. These distinctions aid in initial sample layer number identification.

TEM samples for STEM ADF imaging are prepared by a "direct transfer" [23]. A Quantifoil® TEM grid is placed on the targeted MoS_2 flakes grown on the SiO_2/Si substrate and a drop of isopropyl alcohol (IPA) is placed next to the TEM grid. After the IPA evaporates completely, the SiO_2/Si substrate with the TEM grid is placed into a potassium hydroxide (KOH) solution (∼10%) overnight. After etching away the SiO_2, the TEM grid with MoS_2 flakes is detached from the Si substrate. The TEM grid is then rinsed in de-ionized (DI) water several times. Immediately before imaging, the TEM grid with MoS_2 flakes is annealed in forming gas ($Ar : H_2 = 200$ sccm:50 sccm) at 250 °C for 3 h.

Atomic-resolution STEM ADF imaging is performed on TEAM 0.5, a double-aberration-corrected (scanning) transmission electron microscope (STEM/TEM) located in the National Center for Electron Microscopy (NCEM) at the Molecular Foundry, Lawrence Berkeley National Laboratory. The microscope is here operated at 50 keV to minimize radiation damage to the sample. For STEM ADF imaging, a probe size of ∼1.7 Å, a convergence angle of 32 mrad, and collection angles of 77–385 mrad are used.

Total energy calculations are carried out using density functional theory (DFT) and the projector augmented-wave (PAW) approach as implemented in the Vienna *ab initio* simulation package (VASP) [14,24,25]. The generalized gradient approximation (GGA) of Perdew-Burke-Ernzerhof (PBE) is used to approximate the electronic exchange and correlation. The interlayer van der Waals interactions are considered using a correction scheme by Grimme [26]. We model MoS_2 stacking using a slab model with a vacuum layer of at least 20 Å. All structures are relaxed until the energy has converged to within 10^{-6} eV/unit cell.

III. RESULTS AND DISCUSSION

As a member of transition mental dichalcogenides (TMDs) having rich polytypism [27], bulk MoS_2 presents two commonly observed phases: (1) the 2*H* phase (space group $P6_3/mmc$) which exists naturally and can also be synthesized via chemical vapor transport (CVT) methods, and (2) the 3*R* phase (space group $R3m$) which is typically synthesized (again via CVT methods) [17]. The stacking orders for both 2*H* and 3*R* phases, in the single-layer, bilayer, and trilayer configurations, are shown in Fig. 1. The nomenclature for the stacking sequence used here follows Refs. [14,28]. Single-layer MoS_2 for both phases has the same structure, with one layer of Mo atoms sandwiched between two layers of S atoms. Each layer of Mo and S atoms is arranged in a hexagonal lattice and two S layers have the same in-plane lattice points. For bilayer MoS_2, the 2*H* and 3*R* phases show different stacking sequences for the S-Mo-S sandwiched structure. As shown in Fig. 1, 2*H*-phase MoS_2 in the form of a bilayer has a stacking sequence recorded as AA', with Mo eclipsed over S, and the two layers have inversion symmetry. 3*R*-phase MoS_2 in the form of a bilayer has a stacking sequence *AB*, with staggered Mo over S, and the two layers do not have inversion symmetry. To determine the stacking sequence for trilayer MoS_2 of different phases, we treat the second layer as the first layer (as if it were *A*) and name the stacking sequence for the third layer following the two-layer naming system. Therefore, 2*H*-phase trilayer MoS_2 has a stacking sequence $(AA')A'$ and 3*R*-phase trilayer MoS_2 has the sequence (*AB*)*B*.

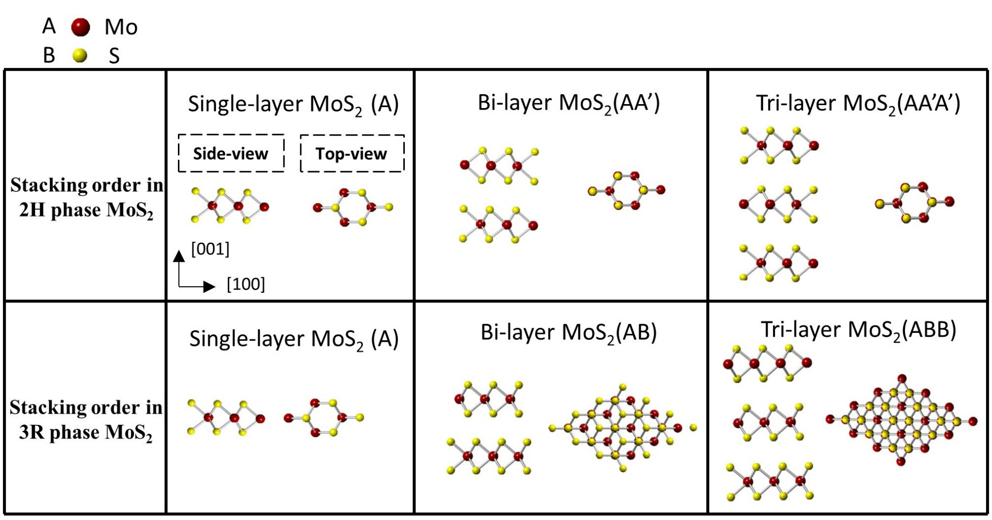

FIG. 1. Schematics showing the stacking orders for 2*H* and 3*R* phases MoS_2 in the single-layer, bilayer and trilayer forms viewed from side and top. Red spheres represent Mo atoms and yellow spheres represent S atoms.

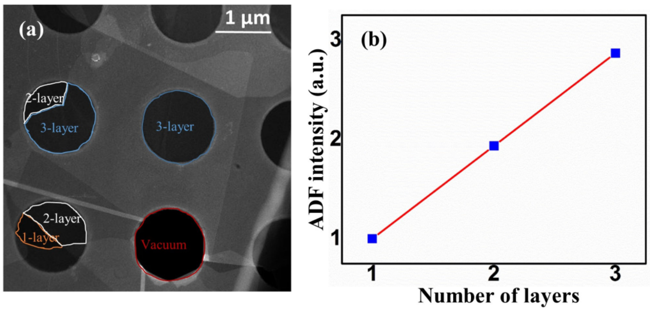

FIG. 2. Low-magnification ADF image of single-layer, bilayer, and trilayer MoS_2. (a) Low-magnification ADF image of the area where one-, two-, and three-layer CVD-grown MoS_2 hang over holes on a Quantifoil® TEM grid. The region of vacuum gives the background counts for the whole image. (b) The intensity in the ADF image is linear as a function of the number of layers after background subtraction using vacuum as reference.

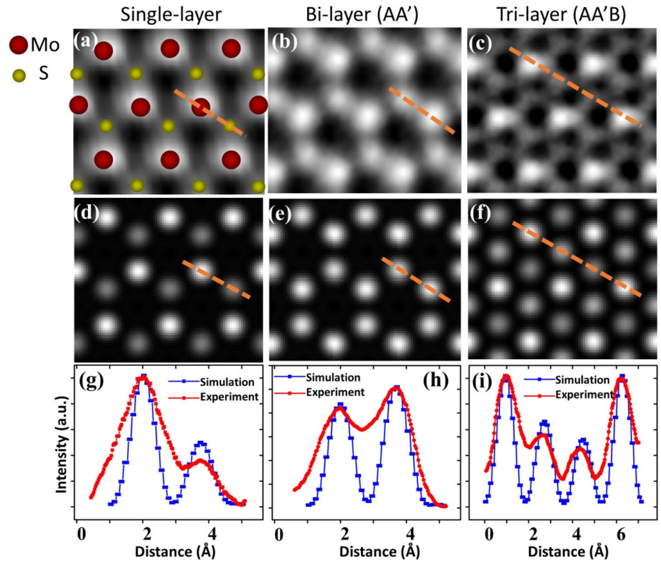

FIG. 3. Atomic-resolution ADF images of single-layer, bilayer (AA' stacking), and trilayer ($AA'B$ stacking) CVD-grown MoS_2 in comparison with simulated images. (a)–(c) Experimentally observed atomic-resolution ADF images of single-layer, bilayer (AA' stacking), and trilayer ($AA'B$ stacking) CVD-grown MoS_2, respectively, after averaging the intensity of more than 10 unit cells from a larger area of the same stacking sequence. (d)–(f) Multislice simulation of ADF images of single-layer, bilayer (AA' stacking), and trilayer ($AA'B$ stacking) MoS_2 with the same beam energy, convergence angle, and collection angles for the experiment. (g)–(i) Line scans across lattice points indicated by the orange lines in (a)–(c) and (d)–(f), showing the comparison of intensity of these lattice points in simulated and experimental ADF images for single-layer, bilayer (AA' stacking), and trilayer ($AA'B$ stacking) CVD-grown MoS_2, respectively.

ADF STEM imaging is a powerful tool to distinguish different atoms provided that the sample has uniform thickness [29]. Given that (1) MoS_2 is composed of two atomic species (Mo and S) which have significantly different atomic numbers (Mo 42, S 16), and (2) multilayer MoS_2 is a layered structure with uniform sample thickness for a certain number of layers, ADF imaging serves ideally to identify the type and location of each atom in thin samples. Figure 2 shows the low-magnification ADF image of single-layer, bilayer, and trilayer MoS_2 suspended over holes of the TEM grid. The layer number can be identified according to the linearly changed intensity in the image after background subtraction (using vacuum as a reference) as shown in Fig. 2(b).

With comparison to simulated ADF images of MoS_2 with known stacking sequences, we identify the stacking sequence in experimental ADF images of CVD-grown few-layer MoS_2. In order to improve the signal-to-noise ratio in the experimentally obtained ADF images, a few or tens of unit cells from a larger sample area are averaged [30] and presented in Figs. 3(a)–3(c), corresponding to single-layer, bilayer, and trilayer MoS_2, respectively [the same region as shown in Fig. 2(a)]. The original ADF images from larger areas of different layer numbers can be found in the Supplemental Material Sec. 2 [22]. Figures 3(d)–3(f) are simulated ADF images based on multislice theory [30]. These simulated images provide information regarding symmetry and relative intensity at different atomic sites for a certain stacking sequence. A match in terms of both symmetry and intensity between simulated and experimental ADF images is essential for the determination of the correct stacking sequence. Experimental ADF images are less sharp than the simulated ones due to incoherence and a broadening effect in the real-life electron probe, as well as drifting effects and sample vibration during the imaging process. In the experimental ADF images, one often finds overlapping of intensity between neighboring atoms, which blurs the atomic edges. The experimental ADF image of single-layer MoS_2 [Fig. 3(a)] shows distinct intensity at two sublattices for Mo and S, respectively, with red spheres representing Mo and overlapping yellow spheres representing S. A simulated ADF image of single-layer MoS_2 [Fig. 3(d)] shows the same symmetry as the experimental ADF image. The line scans across the Mo and S sublattice points in experimental and simulated images [Fig. 3(g)] show the same ratio of relative intensity. With the same analysis method, we find that a great portion (>50%) of bilayer CVD-grown MoS_2 takes the stacking sequence of AA'. An experimental ADF image of such a stacking sequence is shown in Fig. 3(b), in which we consistently observe intensity differences around 15% at two sublattices with threefold symmetry. This is in accord with the multislice simulation shown in Fig. 3(e). The line scans across the inequivalent two lattice points in experimental and simulated ADF images are compared in Fig. 3(h), which show a good match in relative intensity. Nonzero relative rotation angles between the two layers are also observed in our bilayer MoS_2 samples, which are common in CVD-grown MoS_2 (see Supplemental Material Sec. 3 [22] and Ref. [18]).

A new symmetry-breaking stacking sequence is found in our CVD-grown trilayer MoS_2. This stacking sequence is identified to be $(AA')B$ after we compare the experimental and simulated ADF images of trilayer MoS_2 with stacking sequences that have AA' stacking for the first two layers (see Supplemental Material Sec. 4). In $AA'B$ stacked trilayer MoS_2, the third layer is staggered, with S atoms over Mo atoms of the second layer, as shown schematically in Fig. 4(a). There are three distinct lattice points in $AA'B$ stacked trilayer

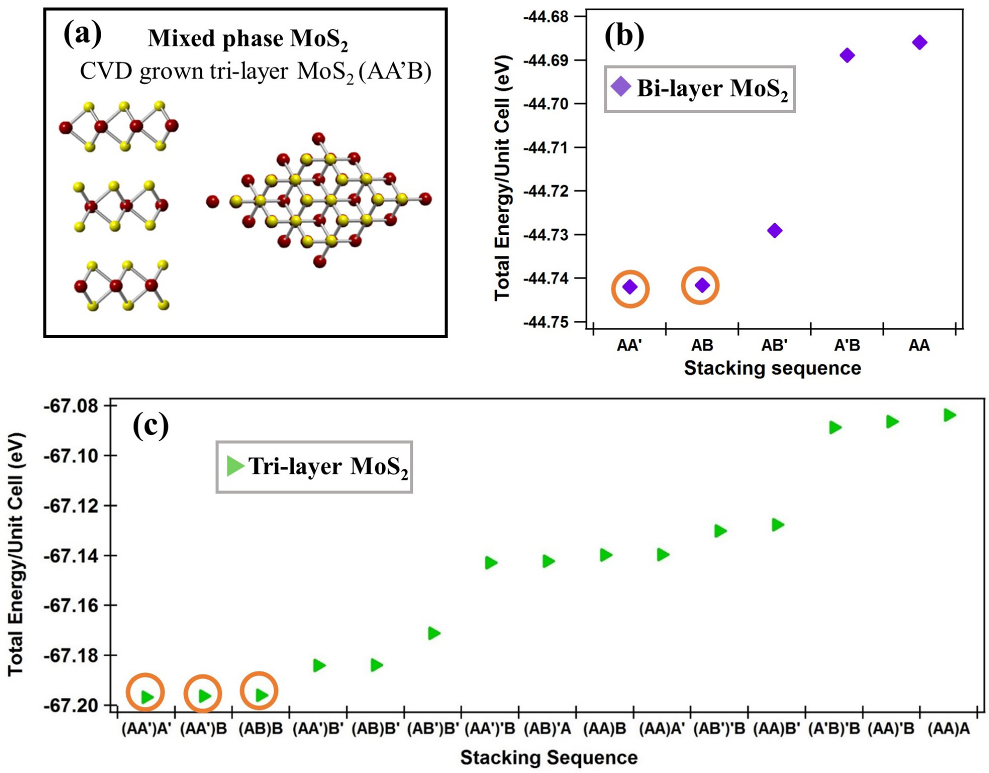

FIG. 4. (a) Crystal structure of trilayer MoS_2 with the stacking sequence $AA'B$ viewed from the side (on the left) and top (on the right); (b) total energies of all possible stacking sequences for bilayer MoS_2, obtained from first-principles calculations; (c) total energies of all possible stable stacking sequences for trilayer MoS_2, obtained from first-principles calculations. Data points outlined by orange circles in (b) and (c) correspond to the stacking sequences with the lowest energies in bilayer and trilayer MoS_2, respectively.

MoS_2, as shown in the experimental [Fig. 3(c)] and simulated [Fig. 3(f)] ADF images. The line scans across these three lattice points [Fig. 3(i)] in experimental and simulated ADF images show that the ratio of intensity for these three lattice points is 1:0.55:0.45 and 1:0.65:0.5, respectively, in reasonable agreement. CVD-grown trilayer MoS_2 with a stacking sequence $AA'B$ is consistently observed (>50%) across the same sample and in samples from different growth batches (see Supplemental Material Sec. 5 [22]).

To understand the prevalence of the $AA'B$ stacking sequence over other stacking possibilities in the trilayer MoS_2, we perform first-principles calculations to study the preference of different stacking sequences of MoS_2. All possible bilayer (five) and trilayer (15) stacking sequences of MoS_2 are calculated and the total energies are compared in Figs. 4(b) and 4(c), respectively (absolute values for all stacking possibilities are in Supplemental Material Sec. 6 [22]). Here, the calculated energy is the total energy from solving the Kohn-Sham equation [31] plus the dispersion corrections by Grimme [26]. For bilayer MoS_2, as expected, the stacking sequences with the lowest energies are AA' and AB, which correspond to bilayer forms of the $2H$ and $3R$ phases, respectively [outlined by orange circles in Fig. 4(b)]. Our calculation results of bilayer MoS_2 are comparable to those of Ref. [14]. These two stacking sequences are close in energy and are commonly observed in experimental studies. In our CVD-grown bilayer MoS_2, AA' stacking is prevalent over AB stacking. Similarly, there are three trilayer stacking possibilities with nearly degenerate calculated energy, as outlined by orange circles in Fig. 4(c): $(AA')A'$, $(AA')B$, and $(AB)B$ (the energy differences are within typical DFT error, so a true ground state is not determined). Importantly, the experimentally observed $(AA')B$ stacking in CVD-grown trilayer MoS_2 is among these predicted minimum energy configurations. Moreover, the $(AA')B$ stacking sequence is dominant in our CVD-grown trilayer MoS_2, and indicates that our growth conditions favor this stacking over other low-energy stacking sequences, probably due to the higher-energy barriers required by those stacking configurations.

CVD-grown few-layer MoS_2 with different stacking sequences reported here is relevant to the electronic and optical properties of this material. Specifically, distinct layer-dependent valley polarization phenomena in few-layer $2H$ and $3R$ phases of MoS_2 [17] suggest that trilayer CVD-grown MoS_2 with mixed stacking sequences ($AA'B$) may present a new valley polarization signature that is different from those of both phases of trilayer form. In addition, we speculate the layer-dependent stacking sequence observed in our CVD-grown few-layer MoS_2 is likely controlled synergistically by various growth parameters. These parameters include growth temperature, feeding rate, and partial pressure of the precursors, which can change slightly over time during the material's nucleation and growth process. Because CVD growth of few-layer MoS_2 follows the so-called "layer-by-layer" growth mechanism [32], the slight change in growth parameters over time will cause a change in the preferred stacking sequence for a certain layer number.

IV. SUMMARY AND CONCLUSIONS

Atomic-resolution STEM imaging is successfully employed to precisely determine different stacking sequences in few-layer CVD-grown MoS_2. The stacking sequences in bilayer and trilayer MoS_2 are found to differ. The 2*H* phase is consistently observed for bilayer CVD-grown MoS_2, which has the stacking sequence AA' with inversion symmetry. The stacking sequence $AA'B$ is observed for the majority of CVD-grown trilayer MoS_2, which shows broken inversion symmetry. First-principles calculations show that the $AA'B$ stacking sequence is among the most stable configurations, with the other two stacking possibilities of $AA'A'$ (2*H* phase) and *ABB* (3*R* phase). Due to the symmetry-breaking nature of trilayer CVD-grown MoS_2, this configuration should be of great interest for valley polarization studies.

ACKNOWLEDGMENTS

This research was supported in part by the Director, Office of Basic Energy Sciences, Materials Sciences and Engineering Division, of the U.S. Department of Energy under Contract No. DE-AC02-05CH11231, within the sp^2-Bonded Materials Program, which provided for postdoctoral support and AFM and PL characterization; by NSF Grant No. DMR-1206512, which provided for the sample growth; and by the Molecular Foundry of the Lawrence Berkeley National Laboratory, under Contract No. DE-AC02-05CH11231, which provided for TEM characterization. We acknowledge Chengyu Song of the Molecular Foundry of the Lawrence Berkeley National Laboratory for TEM technical support. The first-principles modeling work was supported by the Materials Project Center under the DOE Basic Energy Sciences Grant No. EDCBEE.

[1] K. F. Mak, C. Lee, J. Hone, J. Shan, and T. F. Heinz, Phys. Rev. Lett. **105**, 136805 (2010).
[2] A. Splendiani, L. Sun, Y. B. Zhang, T. S. Li, J. Kim, C. Y. Chim, G. Galli, and F. Wang, Nano Lett. **10**, 1271 (2010).
[3] K. K. Kam and B. A. Parkinson, J. Phys. Chem. **86**, 463 (1982).
[4] B. Radisavljevic, A. Radenovic, J. Brivio, V. Giacometti, and A. Kis, Nat. Nanotechnol. **6**, 147 (2011).
[5] O. Lopez-Sanchez, D. Lembke, M. Kayci, A. Radenovic, and A. Kis, Nat. Nanotechnol. **8**, 497 (2013).
[6] Z. Yin, H. Li, H. Li, L. Jiang, Y. Shi, Y. Sun, G. Lu, Q. Zhang, X. Chen, and H. Zhang, ACS Nano **6**, 74 (2011).
[7] M. Buscema, M. Barkelid, V. Zwiller, H. S. J. van der Zant, G. A. Steele, and A. Castellanos-Gomez, Nano Lett. **13**, 358 (2013).
[8] H. S. Lee, S. W. Min, Y. G. Chang, M. K. Park, T. Nam, H. Kim, J. H. Kim, S. Ryu, and S. Im, Nano Lett. **12**, 3695 (2012).
[9] H. Li, Z. Y. Yin, Q. Y. He, X. Huang, G. Lu, D. W. H. Fam, A. I. Y. Tok, Q. Zhang, and H. Zhang, Small **8**, 63 (2012).
[10] D. J. Late, Y. K. Huang, B. Liu, J. Acharya, S. N. Shirodkar, J. Luo, A. Yan, D. Charles, U. V. Waghmare, V. P. Dravid, and C. N. R. Rao, ACS Nano **7**, 4879 (2013).
[11] W. Bao, X. Cai, D. Kim, K. Sridhara, and M. S. Fuhrer, Appl. Phys. Lett. **102**, 42104 (2013).
[12] G.-H. Lee, Y.-J. Yu, X. Cui, N. Petrone, C.-H. Lee, M. S. Choi, D.-Y. Lee, C. Lee, W. J. Yoo, K. Watanabe, T. Taniguchi, C. Nuckolls, P. Kim, and J. Hone, ACS Nano **7**, 7931 (2013).
[13] M. S. Choi, G.-H. Lee, Y.-J. Yu, D.-Y. Lee, S. H. Lee, P. Kim, J. Hone, and W. J. Yoo, Nat. Commun. **4**, 1624 (2013).
[14] J. He, K. Hummer, and C. Franchini, Phys. Rev. B **89**, 075409 (2014).
[15] K. Liu, L. Zhang, T. Cao, C. Jin, D. Qiu, Q. Zhou, A. Zettl, P. Yang, S. G. Louie, and F. Wang, Nat. Commun. **5**, 4966 (2014).
[16] A. M. van der Zande, J. Kunstmann, A. Chernikov, D. A. Chenet, Y. You, X. Zhang, P. Y. Huang, T. C. Berkelbach, L. Wang, F. Zhang *et al.*, Nano Lett. **14**, 3869 (2014).
[17] R. Suzuki, M. Sakano, Y. J. Zhang, R. Akashi, D. Morikawa, A. Harasawa, K. Yaji, K. Kuroda, K. Miyamoto, T. Okuda *et al.*, Nat. Nanotechnol. **9**, 611 (2014).
[18] S. Najmaei, Z. Liu, W. Zhou, X. Zou, G. Shi, S. Lei, B. I. Yakobson, J.-C. Idrobo, P. M. Ajayan, and J. Lou, Nat. Mater. **12**, 754 (2013).
[19] A. M. van der Zande, P. Y. Huang, D. A. Chenet, T. C. Berkelbach, Y. You, G.-H. Lee, T. F. Heinz, D. R. Reichman, D. A. Muller, and J. C. Hone, Nat. Mater. **12**, 554 (2013).
[20] H. P. Komsa, J. Kotakoski, S. Kurasch, O. Lehtinen, U. Kaiser, and A. V Krasheninnikov, Phys. Rev. Lett. **109**, 035503 (2012).
[21] A. Yan, J. Velasco Jr, S. Kahn, K. Watanabe, T. Taniguchi, F. Wang, M. F. Crommie, and A. Zettl, Nano Lett. **15**, 6324 (2015).
[22] See Supplemental Material at http://link.aps.org/supplemental/10.1103/PhysRevB.93.041420 for optical images, Raman spectroscopy and photoluminescence measurement of CVD grown single- and few-layer MoS_2 on SiO_2/Si substrates, large-area ADF images of single-layer, bilayer and trilayer MoS_2, multislice simulation parameters for STEM ADF images, simulated ADF images corresponding to trilayer 3*R* phase MoS_2 and trilayer MoS_2 with the first two layers stacked as AA', and total energies of all possible stacking sequences in bilayer and trilayer MoS_2 by first principles calculations.
[23] W. Regan, N. Alem, B. Aleman, B. S. Geng, C. Girit, L. Maserati, F. Wang, M. Crommie, and A. Zettl, Appl. Phys. Lett. **96**, 113102 (2010).
[24] G. Kresse and D. Joubert, Phys. Rev. B **59**, 1758 (1999).
[25] G. Kresse and J. Furthmüller, Phys. Rev. B **54**, 11169 (1996).
[26] S. Grimme, J. Comput. Chem. **27**, 1787 (2006).
[27] J. A. Wilson and A. D. Yoffe, Adv. Phys. **18**, 193 (1969).
[28] G. Constantinescu, A. Kuc, and T. Heine, Phys. Rev. Lett. **111**, 036104 (2013).
[29] D. B. Williams and C. B. Carter, *The Transmission Electron Microscope* (Springer, Berlin, 1996).
[30] E. J. Kirkland, *Advanced Computing in Electron Microscopy* (Springer, Berlin, 2010).
[31] W. Kohn and L. J. Sham, Phys. Rev. **140**, A1133 (1965).
[32] I. V. Markov, *Crystal Growth for Beginners: Fundamentals of Nucleation, Crystal Growth, and Epitaxy*, 2nd ed. (World Scientific, Singapore, 2003).